Environmental Science Processes & Impacts

ROYAL SOCIETY OF CHEMISTRY

PAPER

View Article Online
View Journal | View Issue

Cite this: *Environ. Sci.: Processes Impacts*, 2021, **23**, 1914

Atmospheric mercury sources in a coastal-urban environment: a case study in Boston, Massachusetts, USA†

Hélène Angot, ‡*[ab] Emma Rutkowski,‡[c] Maryann Sargent,[d] Steven C. Wofsy,[d] Lucy R. Hutyra,[e] Dean Howard,[fg] Daniel Obrist[f] and Noelle E. Selin [ac]

Mercury (Hg) is an environmental toxicant dangerous to human health and the environment. Its anthropogenic emissions are regulated by global, regional, and local policies. Here, we investigate Hg sources in the coastal city of Boston, the third largest metropolitan area in the Northeastern United States. With a median of 1.37 ng m^{-3}, atmospheric Hg concentrations measured from August 2017 to April 2019 were at the low end of the range reported in the Northern Hemisphere and in the range reported at North American rural sites. Despite relatively low ambient Hg concentrations, we estimate anthropogenic emissions to be 3–7 times higher than in current emission inventories using a measurement-model framework, suggesting an underestimation of small point and/or nonpoint emissions. We also test the hypothesis that a legacy Hg source from the ocean contributes to atmospheric Hg concentrations in the study area; legacy emissions (recycling of previously deposited Hg) account for ~60% of Hg emitted annually worldwide (and much of this recycling takes place through the oceans). We find that elevated concentrations observed during easterly oceanic winds can be fully explained by low wind speeds and recirculating air allowing for accumulation of land-based emissions. This study suggests that the influence of nonpoint land-based emissions may be comparable in size to point sources in some regions and highlights the benefits of further top-down studies in other areas.

Received 28th June 2021
Accepted 25th October 2021

DOI: 10.1039/d1em00253h

rsc.li/espi

Environmental significance

This work investigates the sources of mercury, an environmental toxicant dangerous to human health and the environment, in the coastal city of Boston, United States. Using a measurement-model framework, we show that current inventories underestimate mercury emissions in the study area by a factor of 3–7. While emission inventories are thought to be relatively accurate for large point sources, this study adds to the growing body of literature suggesting that fugitive emissions from unknown point and nonpoint sources must be better constrained to improve emission inventories. These emissions are likely to become relatively more important as major point sources are controlled under domestic and global mitigation policies. This study therefore highlights the need of further top-down studies in other regions.

1. Introduction

Mercury (Hg), emitted to air by both natural and anthropogenic sources, can travel through the atmosphere for up to a year before depositing into oceans and lakes where it may accumulate in fish as toxic methylmercury.[1] Globally, human activities released an estimated 1.5 Tg of Hg over the 1510–2010 period (~60% of which have occurred in Europe and North America) and anthropogenic Hg emissions to the atmosphere increased globally by around 20% between 2010 and 2015.[2,3] Current anthropogenic emissions to air are 2.5 ± 0.5 Gg per year.[4] As mercury circulates in the environment for decades or even centuries, legacy emissions (*i.e.*, recycling of previously deposited Hg) add to this atmospheric burden another 4.5–5.6 Gg every year.[4] It is estimated that human activities, including

[a]*Institute for Data, Systems, and Society, Massachusetts Institute of Technology, Cambridge, MA, USA. E-mail: helene.angot@epfl.ch*
[b]*Extreme Environments Research Laboratory, École Polytechnique Fédérale de Lausanne (EPFL) Valais, Wallis, Sion, Switzerland*
[c]*Department of Earth, Atmospheric, and Planetary Sciences, Massachusetts Institute of Technology, Cambridge, MA, USA*
[d]*School of Engineering and Applied Science, Harvard University, Cambridge, MA, USA*
[e]*Department of Earth and Environment, Boston University, Boston, MA, USA*
[f]*Department of Environmental, Earth, and Atmospheric Sciences, University of Massachusetts-Lowell, MA, USA*
[g]*Institute of Arctic and Alpine Research, University of Colorado Boulder, Boulder, CO, USA*

† Electronic supplementary information (ESI) available. See DOI: 10.1039/d1em00253h

‡ These authors contributed equally to the work.

recycled legacy emissions, have increased atmospheric Hg concentrations by ~450%, doubled the Hg stored in organic soils,[5] and tripled the Hg content of surface waters compared to natural levels.[4,6] Due to their detrimental effect on human health and the environment, Hg emissions are regulated by global, regional, and local policies.

The Minamata Convention on Mercury, a global treaty which entered into force in 2017,[7] seeks to control anthropogenic Hg emissions by banning new Hg mines, phasing Hg out of several products and processes, mandating emissions controls on point sources, and regulating small-scale and artisanal gold mining. It also addresses storage, contaminated sites, disposal, and health-risks.[8] As of October 2021, 135 countries have ratified the Convention, including the United States (US).

While Asia is currently the greatest-emitting region,[2,9] anthropogenic emissions of Hg dramatically decreased in the US and North America[10] as a co-benefit of sulfur controls in the 1980s,[1] and later, domestic Hg-specific emission regulations. The US Environmental Protection Agency (EPA) set limits on Hg emissions from coal and oil-fired power plants *via* the Mercury and Air Toxics Standards (MATS) effective in 2015.[11] The emission limitations are technology-based and dictate that all plants must achieve emission reductions as high as the average achieved by the top 12% best-performing facilities. According to the EPA,[12] nationwide Hg emissions decreased by 19 tons from 2014 to 2017, primarily due to lower Hg emissions from electric generating units covered by MATS.

Concentrations of Hg in air in the US have declined together with domestic emission reductions. Based on long-term atmospheric Hg measurements in the Northeastern US, Zhou *et al.*[13] found that concentrations of gaseous elemental mercury (GEM) – the dominant form of Hg in the atmosphere[1] – declined at a rate of 1.8% per year at Underhill (Vermont) from 1992 to 2014, and at a rate of 1.6% per year at Huntington Forest (New York) from 2005 to 2014. Similarly, surface air Hg concentrations in the Northern Hemisphere have declined by 30–40% since 1990,[14–16] at a rate of 1.2 to 2.1% per year in northern midlatitudes.[17] These decreasing trends are consistent with decreased Hg emissions from regional point sources and, in many places, have not been counterbalanced by increasing global emissions.[3] However, some exceptions remain such as Kejimkujik (Nova Scotia, Canada) where the decreasing trend is less than at other North American sites. This lower decreasing trend could result from the balance between the decrease in Hg anthropogenic emissions in the area and potential increases in the release of legacy Hg from the nearby ocean.[18] Although a critical component of the Hg cycle, air–sea exchange is currently poorly constrained due to the lack of direct flux measurements.[19] Understanding how the legacy of past anthropogenic emissions, largely recycled through the oceans, contributes to present-day Hg concentrations is however essential for anticipating the effectiveness of Hg mitigation policies.

Urban centers can also be important sources of GEM due to local fossil fuel combustion and other activities such as metal manufacturing, cement production or water discharges.[1] Fugitive emissions from unknown point and nonpoint sources may also be important in overall urban Hg budgets.[20] Rutter *et al.*[21] showed that nonpoint sources have a higher impact on GEM concentrations than point sources (67% *vs.* 33%, respectively) in Milwaukee, the fifth-largest city in the Midwestern US (~600k inhabitants). In general, there is, however, greater uncertainty in nonpoint sources as these are, by definition, small sources which are not measured directly. While the Minamata Convention aims at the creation of robust emission inventories, more work is needed in urban areas to better characterize sources.[20]

Here, we investigate sources of Hg in the city of Boston (Massachusetts), the third largest metropolitan area in the Northeastern US (~700k inhabitants) using a measurement-model framework. Given the coastal location of the city – located on the shore of the Massachusetts Bay, an inlet of the North Atlantic Ocean – we examine whether legacy Hg evasion from the nearby ocean significantly contributes to observed atmospheric Hg levels. We further evaluate regional anthropogenic Hg emissions in the Greater Boston area and compare emission rates to existing inventories.

2. Material and methods

We installed a GEM monitoring station under the umbrella of the National Atmospheric Deposition Network (NADP) Atmospheric Mercury Network (AMNet) which aims at providing high quality, standardized records of atmospheric Hg concentrations from sites across the US.[22] These measurements along with ancillary data are described in Sections 2.1 and 2.2, respectively. We used two independent but complementary modeling approaches to investigate Hg sources and constrain emissions. The one-box model described in Section 2.3 takes chemical production and loss of GEM into account while the Hybrid Single-Particle Lagrangian Integrated Trajectory (HYSPLIT) inverse analysis (see Section 2.4) tracks a hypothetical conserved tracer. HYSPLIT does, however, account for spatial variability in Hg emissions which cannot be captured in the box model.

2.1 Mercury measurements

The monitoring site was located on the roof of the College of Arts and Sciences building (42.35N, 71.10W) on the campus of Boston University (BU, see Fig. S1†) – near the center of the Boston metropolitan area. The air inlet was placed approximately 1.5 m above the roof, located 29 m above the ground. We used a Tekran 2537A mercury analyzer to monitor ambient air concentrations of GEM from August 2017 to April 2019. The Tekran instrument is commonly used at monitoring sites around the world for measuring atmospheric GEM concentrations.[22,23] Integrated samples were analyzed every 15 minutes at a flow rate of 1 L min^{-1} in order to avoid potential bias in the default integration of the signal by the Tekran instrument.[24–27] An automatic calibration step of the Tekran instrument was carried out every 25 hours with an internal Hg permeation source. The accuracy of this permeation source was annually checked against manual injections of saturated Hg vapor using

a Tekran 2505 Hg vapor calibration unit and a Hamilton digital syringe, and following a strict procedure adapted from Dumarey *et al.*[28] Additionally, the NADP AMNet standard operating procedure was thoroughly followed.

Contrary to the AMNet protocol, we, however, used Millipore 0.45 μm polyether sulfone cation-exchange membranes placed at the entrance of the 15 m-long unheated PTFE sampling line to collect divalent Hg (Hg(II)) species (gaseous and particulate) over two-week periods. This sampling technique has been extensively characterized in laboratory and field experiments (*e.g.*, ref. 29–34). Samples were stored at −8 °C and selected filters ($n = 9$) were analyzed at the US Geological Survey (USGS) Mercury Research Laboratory to determine ambient air divalent Hg concentrations following the analytical procedure described by Marusczak *et al.*[31] Briefly, divalent Hg species were first extracted from each membrane in inverse aqua regia before quantification by cold vapor atomic fluorescence spectrometry. The detection limit was 0.04 ng of Hg per membrane, *i.e.*, an order of magnitude lower than the amount of Hg collected at BU in 2 weeks. Filter blanks were 0.06 ± 0.05 (1σ, $n = 10$), in line with values reported by Marusczak *et al.*[31] In the discussion below, filter blanks were subtracted for all samples.

GEM concentrations in ambient air measured from April 4, 2018 to March 9, 2019 at Harvard Forest (HF) were used as input to our modeling analyses (see Sections 2.3 and 2.4). These measurements were performed in a temperate deciduous hardwood forest at Harvard Forest research station near Petersham, Massachusetts (42.32N, 72.11W), ~110 km west of Boston (see Fig. 1). As described by Obrist *et al.*,[35] GEM was measured on a tower above the forest at heights of 24.1 m and 30.8 m, which were averaged for this study. Sampling lines were 1/4" perfluoroalkoxy (PFA) tubing with 47 mm PFA inlet filter holders and 0.2 μm PFA inlet filters. Inlet filters were changed every one to three months and lines were wrapped for light protection to avoid photochemical reactions. Note that slightly different inlet systems were used at the BU and HF sites. Given the predominance of GEM (90–99%) over other atmospheric Hg species, both at ground-based monitoring sites around the world[23] and in this region of the U.S.,[36] this is not expected to significantly affect the comparison between measurements. The sensitivity of our modeling analyses to GEM concentrations measured at HF is further discussed in Sections 2.3 and S2.†

We further compare GEM concentrations at BU to concentrations monitored at other AMNet sites across the US (see Section 3.1). The data are available at http://nadp.slh.wisc.edu/data/AMNet/, and more information about AMNet sites can be found in Table S1.†

2.2 Ancillary parameters

1 Hz carbon dioxide (CO_2) and methane (CH_4) ambient air mixing ratios were monitored at the BU site using a Picarro G2301 cavity ring down spectrometer (Picarro, Sunnyvale, CA, USA).[37,38] In this paper, we report and discuss CO_2 and CH_4 mixing ratios monitored from August 2017 to April 2019. Sulfur dioxide (SO_2) data were obtained from the Massachusetts Department of Environmental Protection air quality station located in Kenmore Square (KS), located 250 m east of the BU site (see Fig. S1†). Quality controlled SO_2 data were available for a limited time period, from August 2017 to June 2018.[39]

We extrapolated meteorological data from grids produced by NOAA's High Resolution Rapid Refresh (HRRR) model.[40] The HRRR model has a spatial resolution of 3 km and is run every hour using radar data incorporated every 15 minutes, providing hourly data points for wind speed, direction, temperature, precipitation, humidity, snow cover, radiation, and boundary

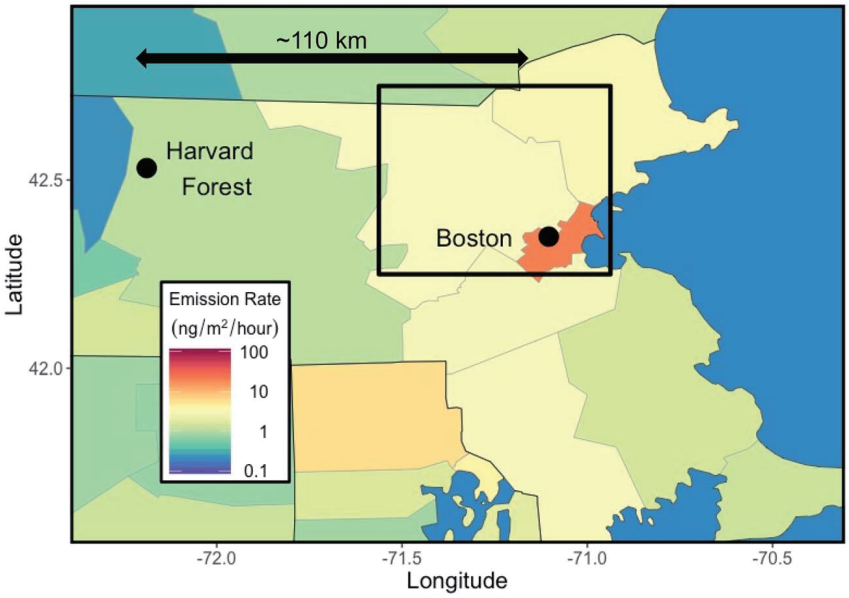

Fig. 1 Location of the atmospheric Hg monitoring stations (Boston and Harvard Forest) relative to the box simulated in the box model, defined by the NASA GMAO Goddard Earth Observing System 0.5 ° × 0.625 ° nested grid(42). The color key gives the aggregated 2014 National Emission Inventory (NEI) anthropogenic emission rate used as anthropogenic emission priors in the box model.

layer height. Observed meteorological data was available from Boston–Logan International Airport, situated ~8 km east of the BU monitoring site (see Fig. S1†). However, the airport is prone to influence from coastal circulations, and thus likely not always representative of conditions at the BU site. We compared the observed Logan Airport data to the HRRR model outputs at the airport and did not find any significant difference (p >0.5) between the two datasets at this point. We therefore considered that the HRRR model provides a reasonable representation of meteorological conditions at the BU monitoring site.

2.3 One-box model analysis

Denzler *et al.*[41] demonstrated the ability of a relatively simple box model to capture GEM concentrations in a localized, urban setting. This box model allowed for calculation of the urban anthropogenic emissions in Zurich, Switzerland. A similar approach is used here, with adjustments to account for local meteorology and sources, in order to estimate ambient air GEM concentrations and constrain anthropogenic and oceanic Hg emission rates.

2.3.1 Model parameterization. The model consists of a single box situated over the Boston metropolitan area (see Fig. 1), with the GEM concentration in the box, C_{box} (in ng m^{-3}), computed by integrating eqn (1) over time (see Fig. 2).

$$\frac{dC_{box}}{dt} = \frac{(E_{soil} + E_{NEI}) \times S + F_{in} - F_{out} - L_{ox} - D_{deposition}}{h \times S} \quad (1)$$

In eqn (1), S is the area of the box, in m^2. The box model area is defined as the area covered by the box encompassing the BU monitoring site in a NASA GMAO Goddard Earth Observing System 0.5 ° × 0.625 ° nested horizontal grid[42] (see Fig. 1). E_{soil} is the rate of re-emission of legacy deposits from the soil in the box, in ng m^{-2} h^{-1}. E_{NEI} is the rate of anthropogenic emission priors in the box (in ng m^{-2} h^{-1}), calculated from the EPA National Emission Inventory[43] (NEI, see Section 2.3.2). F_{in} and F_{out} denote the GEM flux into and out of the box, respectively, due to advection at each time step (in ng h^{-1}). L_{ox} is the amount of GEM removed from the box due to oxidation to divalent Hg, in ng h^{-1}. $D_{deposition}$ is the amount of GEM removed from the box due to dry deposition. Given its negligible nature due to lack of water solubility,[44] wet deposition of GEM was not considered here. h is the height of the box, which is given in meters and is taken to be the height of the planetary boundary layer (variable over time). The detailed parameterization of E_{soil}, L_{ox}, F_{out}, and $D_{deposition}$ can be found in Section S1† and all inputs to the model are summarized in Table S2.†

The flux into the box, F_{in}, depends on wind direction. When winds were blowing from the oceanic sector (wind direction between 30° and 210°), an "ocean flux in" was used, while when winds were from the terrestrial sector (210–30°), a "land flux in" was used. To obtain the land flux, we used the mean of GEM concentrations from HF (see Fig. 1) for each month in which the model was run. This $C_{land\ in}$ represents the regional GEM atmospheric background concentration. The ocean flux in was calculated by solving the differential eqn (2) for GEM concentrations over the ocean, C_{ocean}, assuming uniform concentration across the ocean:

$$\frac{dC_{ocean}}{dt} = \frac{E_{ocean} - D_{ocean}}{h} - L_{ocean} \quad (2)$$

where E_{ocean} is the rate of GEM re-emission priors from the ocean (in ng m^{-2} h^{-1}, see Section 2.3.2), D_{ocean} the amount of GEM lost by dry deposition per unit area of ocean (see Section S1†), and L_{ocean} the amount of GEM lost by chemical oxidation per unit area of ocean (see Section S1†).

For each month, we initialized the model with the first measured GEM concentration of the month, and then ran the

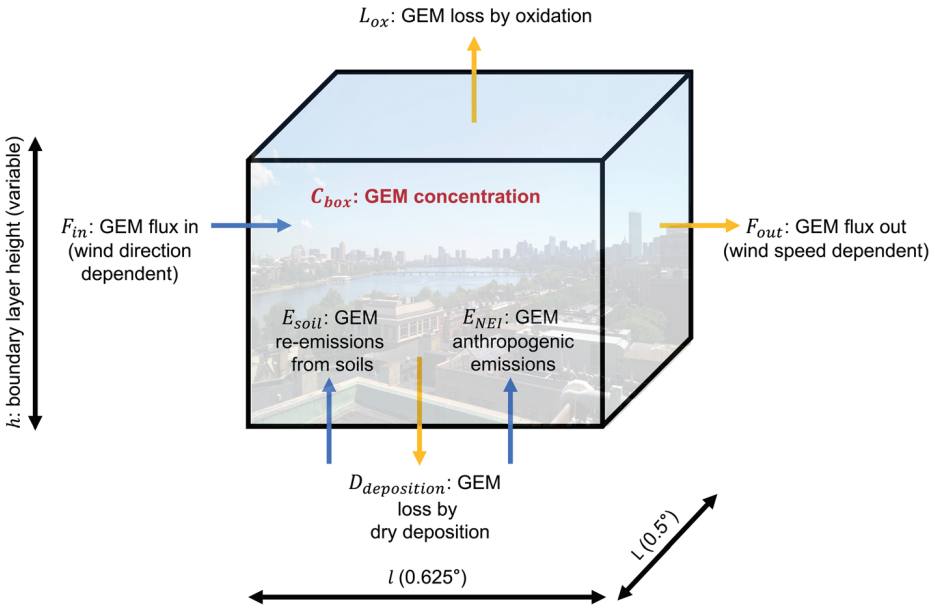

Fig. 2 One-box model structure. The detailed parameterization of the various variables can be found in Section 2.3 of the manuscript and in ESI.†

model for the duration of the month, producing hourly estimates. We applied a 24 hour lowess smoothing function to the model output and the measured concentrations to remove hour-to-hour noise in the time-series – the model was not designed to capture hourly variations due to the size of the box and the use of regionally derived variables. This allowed for a more straightforward analysis of the GEM changes due to wind direction variation occurring on multi-hour timescales. More information on the model sensitivity to the various input parameters can be found in Section S2.†

2.3.2 Emission priors. The 2014 NEI anthropogenic emissions[43] were used as a prior in the one-box model. Note that the recently published 2017 NEI inventory[12] is not significantly different over the region covered by the box model as there are no point sources subject to MATS (implemented in 2015) in the region of interest. County emission rates were calculated by summing the 5 emission types included in the inventory (point, nonpoint, on road, nonroad, event) by county and dividing by the area of the county. The anthropogenic emission rate input into the model was a yearly rate calculated by averaging the county emission rates for all county areas contained within the box model area (see Fig. 1).

Ocean emission priors for year 2015 were obtained by calculating evasion fluxes from prescribed ocean concentrations. The latter were generated using the MITgcm 3D oceanic general circulation model with embedded ecology[45] and currently used as inputs to the chemical transport model GEOS-Chem.[46] The monthly emission rates for the grid box immediately to the east of Boston were taken to constitute the ocean emission priors in the one-box model.

2.3.3 Adjusted emission rates. We used the box model to constrain anthropogenic and oceanic Hg emission rates. The model was run for each month for a combination of oceanic and anthropogenic emission rates. For each run, we calculated a residual by finding the average of the absolute difference between each data point in the measured GEM data series and the model GEM output. The anthropogenic and oceanic emission rates which together minimized the residual for a month were taken to be the best-guess adjusted emission rates for that month. We repeated the same process with $C_{\text{land in}}$ adjusted to $\pm$25% in order to get upper and lower bounds on the adjusted emission estimates (see sensitivity analysis, Section S2†). The model performance at reproducing GEM concentrations measured at BU using prior and adjusted emission rates is discussed in Section 3.2.2.

2.4 HYSPLIT inverse analysis

An independent assessment of Hg emissions was performed using the HYSPLIT model[47] in STILT (Stochastic Time-Inverted Lagrangian Transport) mode in a top-down framework that has been described by McKain *et al.*[48] and Sargent *et al.*[38]

In this analysis, we modeled changes in the GEM concentration as air traveled to the BU site from the edge of a 90 km radius circle centered at BU. The modeled increase in GEM above the concentration at the region boundary (ΔGEM) was determined using HYSPLIT coupled with a prior estimate of GEM emissions. The HYSPLIT model released an ensemble of 500 particles at each hour at BU and followed their trajectories backwards in time based on wind fields and turbulence from the HRRR model (see Section 2.2). HYSPLIT generates an influence function known as the "footprint" (units: mole fraction of Hg per unit flux for each grid square) which quantifies how upwind surface fluxes lead to changes in GEM concentration at the receptor site. In the near-field, the mixing layer height in HYSPLIT was adjusted based on the particle heights as described in Sargent *et al.*[38] to better account for the particles' interaction with the surface before they are fully mixed through the planetary boundary layer.

As the amount and spatial distribution of GEM emissions are not well-constrained, we compared two different prior estimates of emissions ("Zones" and "ACES", see Fig. S2†) to assess their impact on calculated top-down emissions. The two estimates include emissions of 0.6 ng m^{-2} h^{-1} over the ocean (adjusted emission rate, see Section 3.2.2), with different emission estimates over land. In contrast to the box model which attributes constant emissions over the 0.5 ° × 0.625 ° box (see Section 2.3), "Zones" assumes that both current and legacy emissions are more concentrated in the more densely populated area in and around Boston, and roughly matches the emissions from NEI 2014 shown in Fig. 1. The "Zones" estimate attributes Hg emissions of 20 ng m^{-2} h^{-1} over land within a 10 km radius of Boston, with emissions of 3 ng m^{-2} h^{-1} elsewhere over land. The second prior, "ACES", is based on anthropogenic CO_2 emissions from the 1 km resolution Anthropogenic Carbon Emissions System (ACES) inventory,[49] which includes all major carbon-emitting sectors using an extensive database of high-resolution spatial proxies. Assuming that Hg emissions are generally co-located with current or past CO_2 emissions, this prior scales the ACES inventory such that regional total emissions are equal to Hg emissions from NEI 2014. The convolution of the HYSPLIT footprint within our study region with prior emissions produced ΔGEM, the expected increase in GEM concentration between our study boundary and urban measurement site based on the prior emissions estimate.

The GEM concentration at the boundary of the study region for each day was calculated as the mean of GEM measurements from 10 : 00 to 17 : 00 Eastern Standard Time (EST) at the HF site (regional background concentration). In calculating inverse emissions, we only used trajectories with winds from the SW to NW (exit azimuth 200–350°) for which the HF site is representative of background concentrations (note that the ocean emissions analysis below used all exit angles). The observed ΔGEM was calculated as the difference between the observed GEM concentration at BU and the background from HF, with a time delay between the upwind and downwind sites equal to the average travel time from the receptor to the study region boundary. Hourly average ΔGEM were aggregated into daily afternoon averages (11:00 to 16:00 EST) to focus on periods when the atmosphere is well-mixed.

A single scaling factor was determined for each season by dividing the mean observed GEM enhancement by the mean modeled GEM enhancement:

$$SF = \text{mean}(\Delta GEM_{obs})/\text{mean}(\Delta GEM_{\text{model prior}}) \quad (3)$$

Optimized GEM emissions were calculated as the product of the prior emissions and the SF for each time period, with no adjustment to the spatial distribution of the prior.

We also used the HYSPLIT model to assess the impact of ocean emissions on observed GEM concentrations in Boston. For this analysis, we separated our model ΔGEM into land and ocean components, and calculated separate scaling factors for each component to best match the observed ΔGEM:

$$\Delta GEM_{\text{model opt}} = \Delta GEM_{\text{land model}} \times SF_{\text{land}} + \Delta GEM_{\text{ocean model}} \times SF_{\text{ocean}} \quad (4)$$

As land influence dominated our footprint, we first optimized GEM emissions over land for days primarily influenced by land emissions, with particle exit angles of 200–350° as well as less than 10% of the total footprint over ocean grid cells. For days with negligible ocean influence:

$$SF_{\text{land}} = \text{mean}(\Delta GEM_{obs})/\text{mean}(\Delta GEM_{\text{land model}}) \quad (5)$$

where $\Delta GEM_{\text{land model}}$ is equal to the product of prior land emissions and the HYSPLIT footprint. Having calculated SF_{land}, we then subtracted optimized land ΔGEM from observed ΔGEM to calculate SF_{ocean} for days with a significant ocean footprint:

$$SF_{\text{ocean}} = \text{mean}(\Delta GEM_{obs} - \Delta GEM_{\text{land model}} \times SF_{\text{land}})/\text{mean}(\Delta GEM_{\text{ocean model}}) \quad (6)$$

In this way we separated model land and ocean emissions to examine the magnitude of the ocean source.

3. Results and discussion

3.1 GEM time-series and comparison to other AMNet sites

Fig. 3a shows the time-series of hourly-averaged GEM concentrations recorded over the course of this study at the BU monitoring site. This time-series is characterized by day-to-day fluctuations and occasional spikes which never exceeded 5 ng m^{-3}. These spikes could suggest long-range transport of Hg. We did not, however, find any indication of regular pollution transport from other states (see Section S3†), which is in line with the infrequent nature of these spikes. As shown in Fig. S3,† summer GEM concentrations (1.32 ± 0.28 ng m^{-3}; median ± interquartile range here and throughout the manuscript) were slightly lower than in winter (1.40 ± 0.12 ng m^{-3}), with the exception of July. The July 2018 GEM maxima can likely be attributed to smoke from Siberian wildfires which was transported to the Northeastern US.[50] This hypothesis is supported by the Whole Atmosphere Community Climate Model[51] CO forecast simulations, available at https://www.acom.ucar.edu/waccm/forecast/, and showing enhanced CO surface mixing ratios over New England states at that time.

The seasonality observed at BU contradicts that at other urban sites in North America and Asia, but is in line with that at Northern Hemisphere background sites.[52] Building on observations at 50 global sites, Jiskra *et al.*[52] showed that the seasonality at urban sites is generally driven by that of anthropogenic emissions, while the seasonality at other sites is consistent with seasonality driven by plant stomatal uptake. The authors further showed that an oxidation-driven GEM seasonality is not consistent with constant year-round GEM levels in the Southern Hemisphere. The fact that the seasonality observed at BU contradicts that at other urban sites could suggest relatively low local anthropogenic emissions (see below) and/or a significant vegetation control on atmospheric GEM concentrations. While being the 3rd most densely populated US state, Massachusetts is heavily forested (62% forest cover) and is the 8th most forested state in the country.

With a median value of 1.37 ± 0.20 ng m^{-3}, GEM concentrations recorded in Boston were at the low end of concentrations reported in the Northern Hemisphere.[23] Fig. 4 shows a comparison between GEM concentrations in Boston and at other AMNet sites across the US. GEM concentrations in Boston are within the range of values reported at rural sites (1.38 ± 0.22 ng m^{-3}, in orange) and significantly (p-value <0.01) lower than at other urban sites (1.69 ± 1.32 ng m^{-3}, in red). Divalent Hg

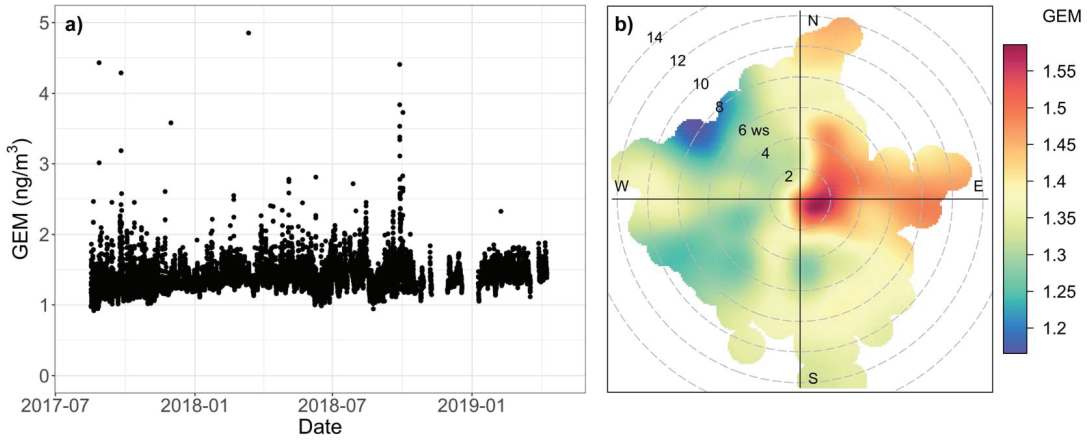

Fig. 3 (a) Time-series of hourly-averaged GEM concentrations recorded in Boston from August 2017 to April 2019. (b) Median GEM concentration (in ng m^{-3}) by wind speed (in m s^{-1}) and direction.

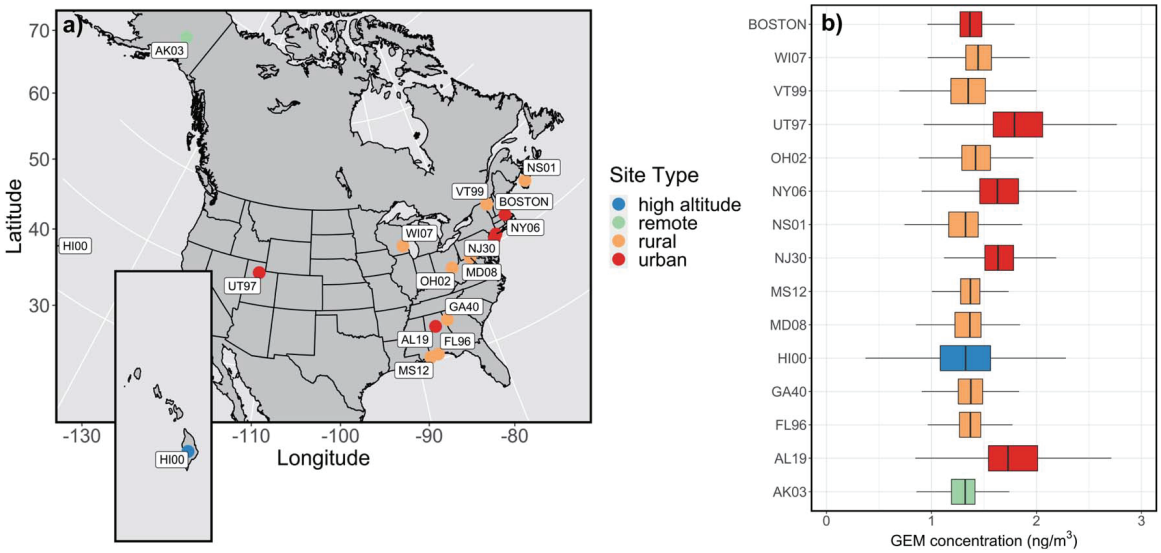

Fig. 4 Comparison of GEM concentrations in Boston *vs.* other AMNet sites. Blue, green, orange, and red dots/boxplots refer to high altitude, remote, rural, and urban sites, respectively, according to the classification made by Gay *et al.*[22] (a) Location of the various sites. More information about AMNet sites can be found in Table S1.† (b) Boxplot of GEM concentrations at the various sites. The vertical black line represents the median. The lower and upper ends of the box correspond to the first and third quartiles (25th and 75th percentiles). The upper (lower) whisker extends from the box to the largest (smallest) value no further than 1.5 × IQR, where IQR is the inter-quartile range.

concentrations, quantified from the use of cation-exchange membranes over two-week periods, ranged from 11.8 to 21.5 pg m^{-3} and did not exhibit any clear seasonal pattern (see Table 1). We, however, acknowledge that the number of samples analyzed might not be sufficient to discern a seasonal pattern. These divalent Hg concentrations are significantly lower than observations at other urban sites (*e.g.*, ref. 53–55) but in the range of values reported from remote sites in the Northern Hemisphere (*e.g.*,ref. 31 and 56–58).

The relatively low GEM and divalent Hg concentrations reported here suggest remoteness from large emission sources. Hg emissions by New England states (Maine, Vermont, New Hampshire, Massachusetts, Connecticut, and Rhode Island) are at the low end of US state-level Hg emissions.[59] In 1998, New England States, the Atlantic Provinces, and Québec adopted a regional Hg action plan with aggressive emission reduction goals.[60] The Northeast States for Coordinated Air Use Management (NESCAUM) estimated that Hg air emissions in Massachusetts were reduced by over 90% from 1996 to 2008.[61] According to NESCAUM, municipal waste combustors are the largest remaining single source sector for Hg emissions in Massachusetts (39.9%). Other emission sources include sludge incinerators, crematoria, electric lamp breakage, and general lab use.[61] It should be noted that all medical waste incinerators have been closed since 1996[61] and that the last coal-burning power plant in Massachusetts shut down in 2017.[62] Unlike Boston, other urban AMNet sites (see Fig. 4) are located closer to large Hg emission sources. UT97 is located in the high Utah desert, within the urbanized metropolitan air shed of Salt Lake City and downwind of the greatest single concentration of gold mining Hg sources in the US.[22,63] NY06 is located in the heart of New York City,[22] and numerous large sources of Hg surround AL19 (Birmingham, Alabama).[64] Finally, the New Brunswick site in New Jersey (NJ30) is located downwind of a known large Hg source – an electric-arc steel manufacturing plant.[65]

Table 1 Divalent Hg concentration (in pg m^{-3}) on selected cation-exchange membranes placed at the entrance of the sample line over two-week periods at the BU site

Start date	End date	Divalent Hg (pg m^{-3})
August 30, 2017	September 13, 2017	16.0
September 13, 2017	October 2, 2017	16.5
October 2, 2017	October 16, 2017	13.5
January 10, 2018	January 24, 2018	21.5
February 23, 2018	March 9, 2018	18.4
April 6, 2018	April 20, 2018	11.9
May 22, 2018	June 5, 2018	16.0
June 19, 2018	July 3, 2018	19.8
July 18, 2018	August 1, 2018	21.4

In order to better understand the fluctuations observed in the GEM time-series (see Fig. 3a) and the relative contribution of local and regional sources, we investigated how GEM concentrations varied by wind speed and direction. Fig. 3b indicates higher median GEM concentrations under low wind speed (<5 m s^{-1}) – suggesting local source contributions, and when easterly winds prevailed. These two source regions were further investigated and are discussed in the following sections.

3.2 Local anthropogenic emission rates

Fig. 5a shows the influence of wind direction (10° bins) and wind speed (2.5 m s^{-1} bins) sectors to the overall mean GEM concentration at BU. We find that measurements carried out when wind speeds were below 2.5 m s^{-1} occurred on 46% of the

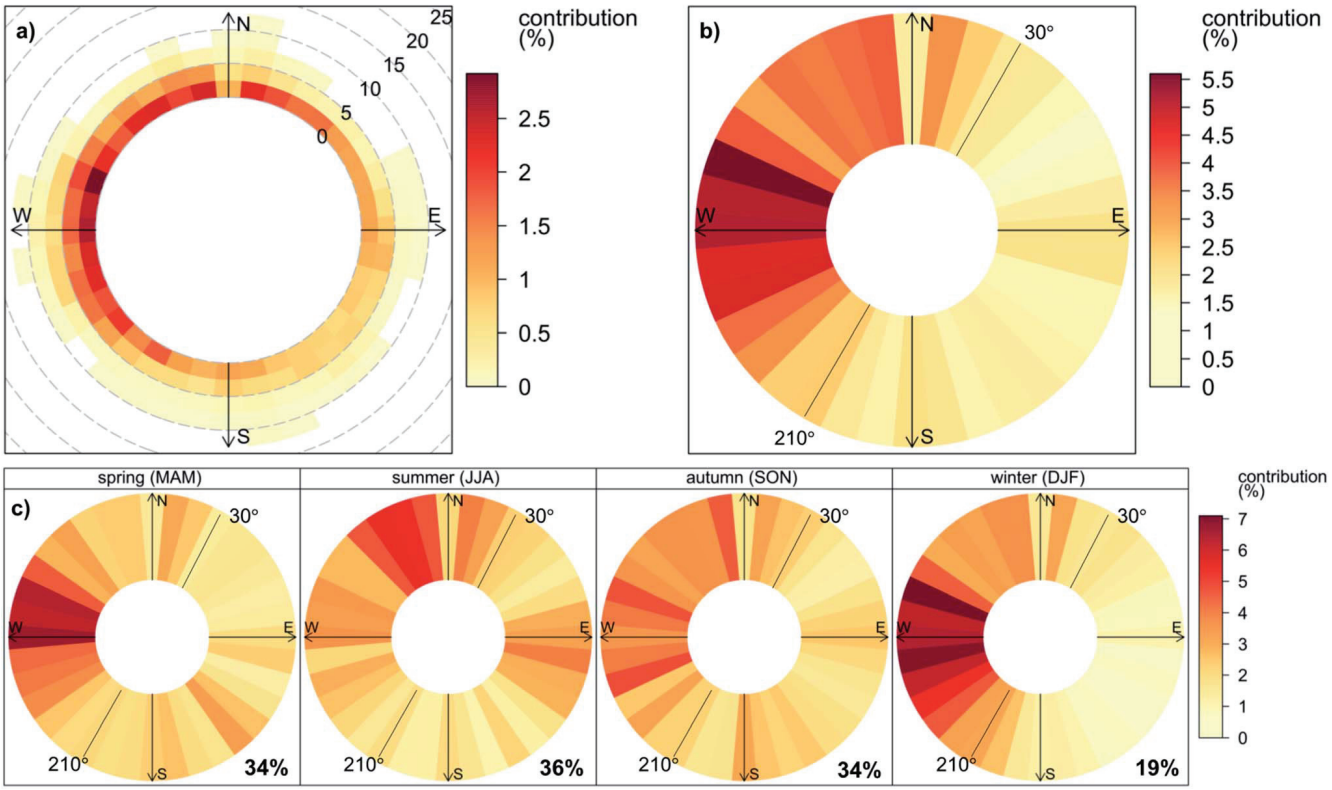

Fig. 5 Contribution of measurements binned by (a) wind direction (10° bins) and wind speed (2.5 m s^{-1} bins), (b) wind direction only, (c) same as b but per season to the annual mean GEM concentration at BU. For instance, panel (b) shows that GEM concentrations at BU are predominantly influenced by measurements performed when the wind blew from the western sector. The numbers in bold at the bottom right represent the contribution of the oceanic sector (30–210°). This figure was made using R package openair.[87]

sampling days but contributed 58% to the overall GEM mean, while measurements carried out when wind speeds were below 5 m s^{-1} occurred on 74% of the sampling days but contributed 91%. The large contribution of measurements under low (<5 m s^{-1}) wind speeds to mean GEM ambient levels suggests the existence of local emission sources.

3.2.1 Hg emission rates based on observed GEM to CO_2 ratios. CO_2 and CH_4 ambient mixing ratios measured at the BU monitoring site can be used as proxies for fossil fuel emissions, particularly in the dormant season, when biological sources of both gases are at a minimum. Using ethane to methane ratios measured at our BU site, McKain *et al.*[66] found that natural gas accounted for 92% of observed CH_4 during the dormant season, while Sargent *et al.*[38] found that anthropogenic CO_2 emissions accounted for 95% of model CO_2 in Boston during the dormant season. Based on our measurements, while CO_2 and CH_4 were strongly and positively correlated (R^2 ~0.8, p <0.001), GEM was moderately (R^2 ~0.4, p <0.001) correlated to CO_2 and CH_4, suggesting that these compounds share some (*e.g.*, fossil fuel burning[1]), but not all, of their sources.

We calculated average anthropogenic GEM emissions in Boston in the winter using GEM to CO_2 ratios observed at the BU site. This analysis assumes that most current and legacy GEM emissions are spatially distributed similarly to current CO_2 combustion emissions. We limit our analysis to winter (December to February), when the biological CO_2 flux is low, and to measurements made during the day when the atmosphere is turbulent and relatively well-mixed (11:00 to 16:00 EST). We found a positive correlation between GEM and CO_2 at BU (R^2 ~0.6, p <0.001), and the regression slope indicates the emission of 0.015 ± 0.001 g of Hg per ton of C (p <0.001) in the Boston metropolitan area (see Fig. 6a). Lee *et al.*[67] similarly compared CO_2 and GEM measurements from June 1999 to May 2000 in Connecticut, and reported emissions of 0.094 ± 0.004 g of Hg per ton of C. The significantly lower emission ratio reported here could be attributed to the anthropogenic emission reductions under the 1998 regional Hg action plan (see Section 3.1) and/or to changes in fuel types in the region. Multiplying the slope of the observed GEM to CO_2 ratio (0.015 ± 0.001 g of Hg per ton of C) by the winter ACES CO_2 emissions of 1781.9 kg per C per km^2 per h produces estimated GEM emissions of 25.0–28.5 ng m^{-2} h^{-1}.

We further investigated the impact of traffic on GEM concentrations. In winter, the rush hours are apt to occur while the atmosphere is stratified (*i.e.*, emissions are trapped within the inversion layer) and provide a test for the null hypothesis: if GEM does not correlate with CO_2, then Hg does not come from traffic. Using only wintertime data between 6:30–9:00 and 16:00–18:00 EST we found a positive correlation between GEM and CO_2 at BU (R^2 ~0.7, p <0.001) and the regression slope indicates the emission of ~0.008 g of Hg per ton of C (p <0.001; see Fig. 6b). These results indicate that traffic is one of the

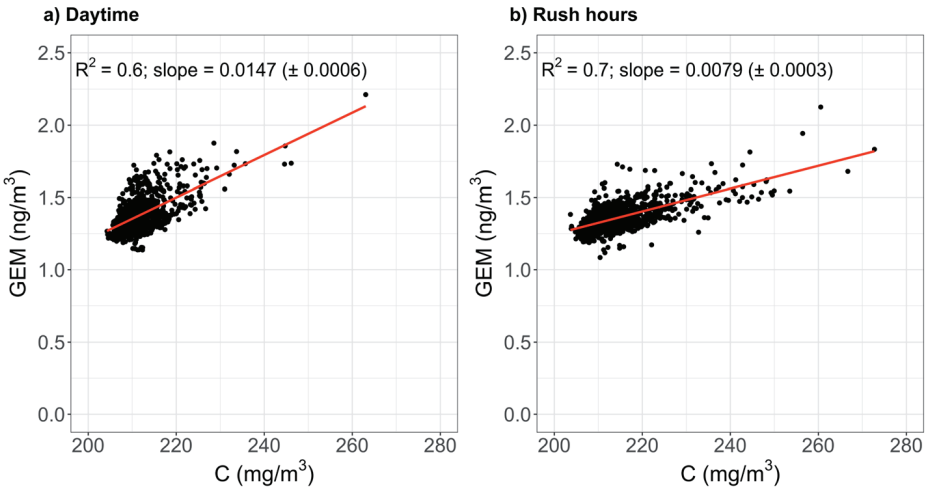

Fig. 6 Scatter plot of wintertime (December to February) GEM and CO_2 concentrations (as mg C per m^3) during (a) daytime (11:00 to 16:00 Eastern Standard Time), and (b) rush hours (6:30 to 9:00 and 16:00 to 18:00 Eastern Standard Time). Also shown are regression line (in red), coefficient of determination (R^2), and slope of the regression line (±standard error of estimate).

contributing Hg sources but not the dominant one (the slope is ~half of the daytime average). According to Conaway *et al.*,[68] the combustion of gasoline and diesel contributes 0.7–13 kg of Hg per year in the San Francisco Bay area, *i.e.*, less than 3% of total emissions. Similarly, residential heating only contributes 4 kg of Hg per year according to the 2011 Massachusetts inventory.[61] This is in good agreement with the emission inventory performed for the latest Global Mercury Assessment:[3] stationary combustion of oil, gas, and biomass contributes 3.0% of global Hg emissions while domestic and residential burning contributes 2.6%.

3.2.2 Hg emission rates based on the box model. We used our box model as an independent estimate of anthropogenic emission rates. Following the methodology described in Section 2.3.3, we adjusted anthropogenic emission rates in the 0.5 ° × 0.625 ° box encompassing the BU monitoring site from 4.2 ng m^{-2} h^{-1} to 8.1–13.7 ng m^{-2} h^{-1} (annual average emission rate over the ~3850 km^2 box), and oceanic emission rates from 0.2 to 0.6–0.7 ng m^{-2} h^{-1} (annual mean). The increased ocean emission rate is consistent with recent work from Zhang *et al.*[69] which found global net GEM evasion to be higher when using a more physically representative version of GEOS-Chem coupled to the MIT global ocean circulation model, as compared to the offline version (emission priors), and within the range of values expected along the northeastern coast of the US.[69] The NEI emission inventory (anthropogenic emission priors) is expected to underpredict emissions as it does not necessarily include all the sources in the Boston area: facilities are required to report emissions to NEI only if their emission is above a certain threshold, leaving the potential for underestimating small point and nonpoint sources. Emissions from Hg-added products (*e.g.*, certain types of batteries, switches, relays, lamps, pesticides, cosmetics) are for instance difficult to quantify as commercial Hg enters the environment either during use or following product disposal.[70] Our findings are in good agreement with observations during the NOMADSS aircraft campaign, which also demonstrated an underestimation of emissions to air in the NEI emission inventory.[71,72]

The model performance at reproducing day-to-day variability of GEM concentrations measured at BU using prior and adjusted emission rates from the box model can be seen in Fig. 7. In general, when run with the emission priors, the model tended to underestimate GEM concentrations. The adjusted emissions provided a better fit (within 10% of observations) and better reproduced the day-to-day variability of GEM concentrations. The correlation coefficients and residual values for observations and model estimates using prior and adjusted emissions are given in Table S4.† Correlation coefficients were much improved using adjusted emission rates, although correlation remained low particularly in the summer and fall months likely due to the fact that the model does not account for the seasonality of plant uptake of GEM.[52]

Our box model analysis suggests higher Hg emissions during the dormant season (November to March, 10–16 ng m^{-2} h^{-1}) than during the growing season (May to September, 6–11 ng m^{-2} h^{-1}). As mentioned above, the seasonality of GEM concentrations is influenced by plant uptake. However, the seasonality of this sink is not accounted for in the model (constant dry deposition velocity, see Table S2†). If this effect was included in the model, we would expect summertime emission rates to be higher to compensate for increased loss, and less of an apparent seasonal cycle in the anthropogenic emissions. Considering this limitation, we suggest 10–16 ng m^{-2} h^{-1} as the more likely range for Hg emissions throughout the year.

3.2.3 Hg emission rates based on the HYSPLIT inverse model. As a third, independent assessment, we calculated GEM emissions using the HYSPLIT analysis described in Section 2.4. Note that unlike the box model, this analysis takes the spatial variability of GEM emissions into account. For each of the two spatial distributions described (see Fig. S2†), we calculated a single multiplicative scaling factor which was multiplied by

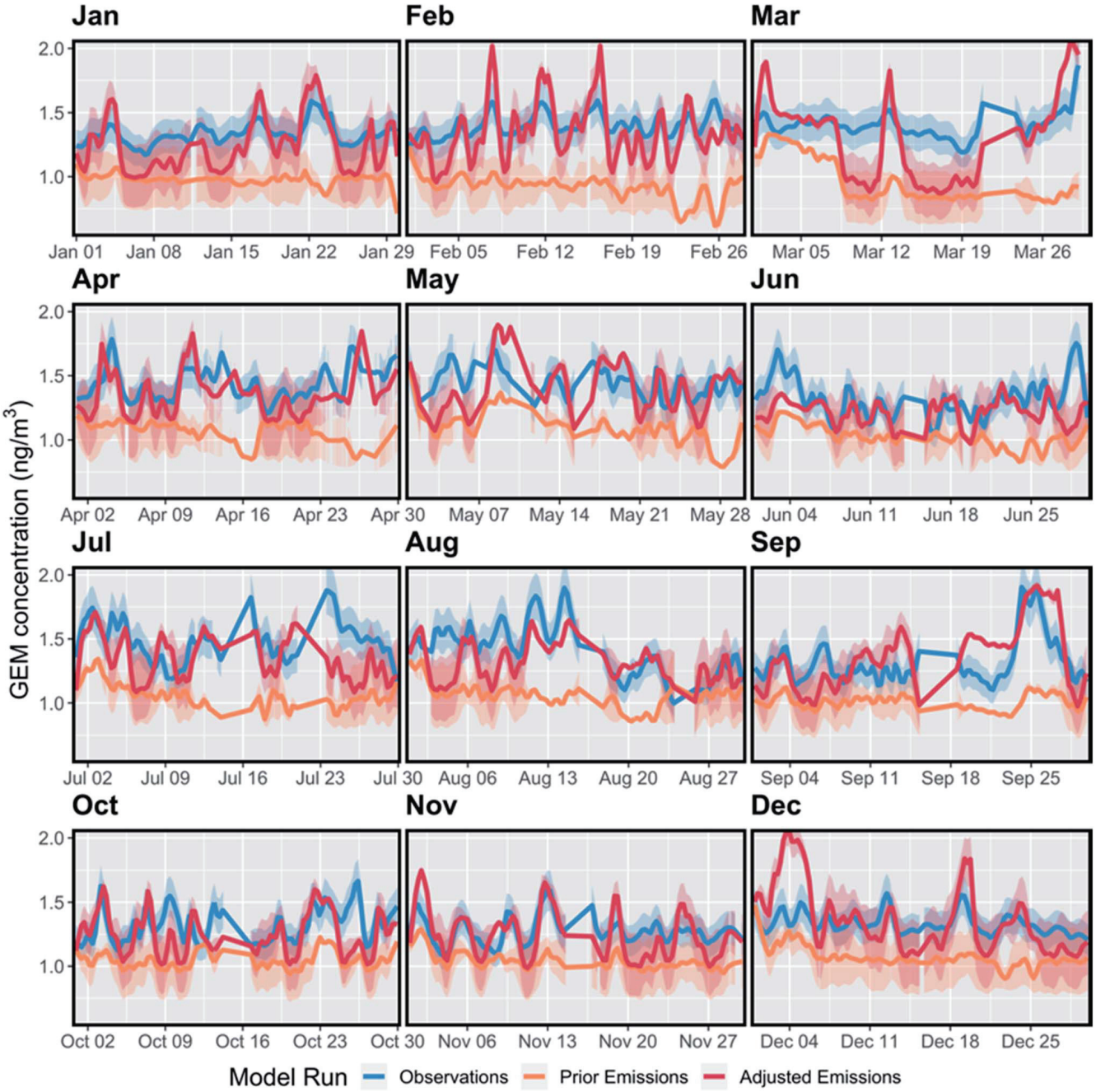

Fig. 7 Timeseries of GEM concentrations measured in Boston ("Observations", in blue) with a 10% analytical uncertainty (blue shaded region), and results of the box model runs using emission priors (in orange) or adjusted emissions (in red). Orange and red shaded regions represent the error due to *a* ±25% variation in $C_{land\ in}$ (see Section S2†).

the prior emissions to best match the observed atmospheric GEM concentrations. Average emission rates over the 0.5 × 0.625° box model study area and over the 90 km region from BU to HF are shown in Table 2. Annual average emissions over the box model study area ranged from 22 to 29 ng m^{-2} h^{-1} with the "ACES" and "Zones" spatial distributions, respectively. These values are in line with the emission rates inferred from the observed GEM to CO_2 ratio (25.0–28.5 ng m^{-2} h^{-1}; see Section 3.2.1) and at the upper end of adjusted emissions with the box model (10–16 ng m^{-2} h^{-1}; see Section 3.2.2).

In summary, all three independent methods (GEM to CO_2 ratio, box model, HYSPLIT model) produce emissions 3–7 times larger than the prior estimate from NEI (4.2 ng m^{-2} h^{-1}), suggesting an underestimation of Hg emissions in current inventories. As discussed in Section 3.2.2, the NEI likely underestimates small point and nonpoint sources. According to the NEI, most Hg emitted in Massachusetts comes from nonpoint rather than point sources due to past and ongoing mitigation policies targeting large point sources. On a national scale, nonpoint emissions currently account for ~25% of US

Table 2 Prior and posterior average GEM emissions based on the HYSPLIT analysis in ng m^{-2} h^{-1} over the 0.5 × 0.625° study area shown in Fig. 1 ("box") or 90 km-radius circle centered on BU site (see Fig. S2) for all data, dormant season (Nov–Mar) and growing season (May–Sept)

	Prior box	Posterior box	Dormant posterior box	Growing posterior box	Posterior 90 km radius circle
Zones	4.3	29	29	27	20
ACES	5.3	22	24	20	11

annual Hg emissions according to the latest NEI inventory. Assuming a nation-wide factor of 3 underestimation, nonpoint sources could potentially equal point sources in terms of annual Hg emissions. This back-of-the-envelope calculation warrants further studies to better constrain Hg inventories in other regions.

3.3 Oceanic source region

Observed GEM concentrations at BU were significantly higher (p <0.001) during times of oceanic winds (30–210°, 1.45 ± 0.25 ng m^{-3}) compared to terrestrial winds (1.34 ± 0.17 ng m^{-3}), as shown in Fig. 3b. Despite a slight underestimation of GEM concentrations, box model runs with adjusted emissions were

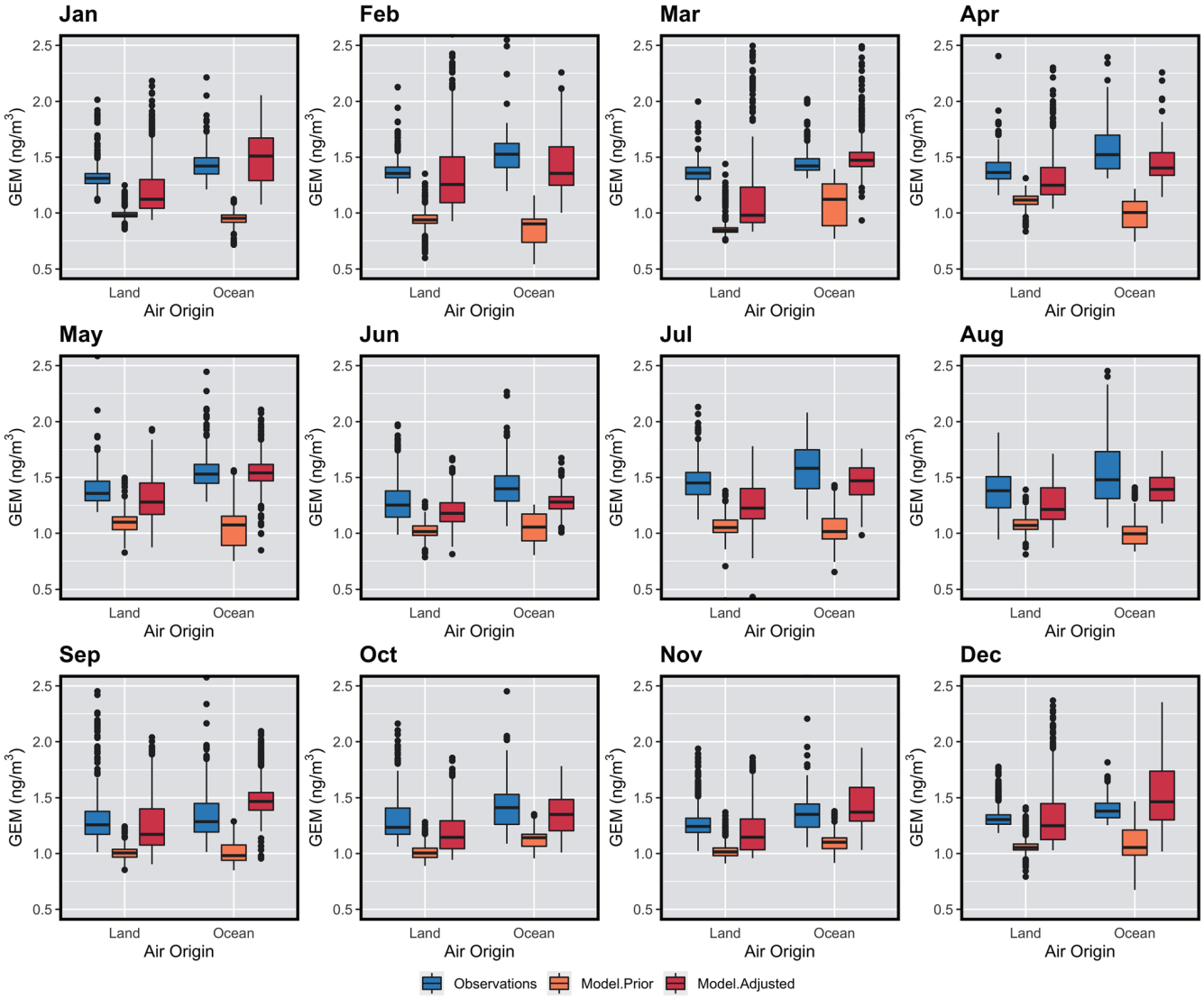

Fig. 8 Monthly boxplots of GEM concentrations in terrestrial and oceanic air masses. Observations at BU are in blue while concentrations predicted by the box model when run with the emission priors or adjusted emissions are given in orange and red, respectively. The lower and upper ends of the box correspond to the first and third quartiles (25th and 75th percentiles). The upper (lower) whisker extends from the box to the largest (smallest) value no further than 1.5 × IQR, where IQR is the inter-quartile range.

able to reproduce higher GEM concentrations in oceanic *vs.* terrestrial air masses (Fig. 8). It should, however, be noted that terrestrial winds prevail in Boston and the mean GEM concentration at the BU site was mostly influenced by the western sector. Fig. 5b shows the percentage contribution of measurements binned in 10° wind direction segments to the overall mean GEM concentration at BU: measurements when the wind blew from the oceanic sector (30–210°) contributed only 34% (annual average) to the overall mean. The influence of the oceanic sector (30–210°) was markedly higher in spring, summer, and fall compared to winter (34–36% *vs.* 19%, see Fig. 5c).

The marked difference in GEM concentration as a function of wind direction prompted us to explore the sources of GEM emissions during oceanic winds. Potential sources include ship exhaust, reemission of legacy Hg from the ocean, or land emissions recirculating due to the sea breeze effect.

Several studies have reported that ship exhaust is a likely source of Hg.[73–76] The Port of Boston, located in Boston Harbor, to the east of BU (see Fig. S1†), is a major seaport. We explored whether ship exhaust could explain the easterly source identified in Fig. 3b by calculating correlations with SO_2, as the cargo fleet accounts for 6–12% of global anthropogenic sulfur emissions.[77,78] However, we found a very weak correlation ($R^2 = 0.13$, p <0.001), and no evidence that ship exhaust is a significant source of GEM.

The oceanic source region could also suggest release of legacy Hg from the ocean. This hypothesis is consistent with GEM observations at a background site in Nova Scotia where air originating from the Northwest Atlantic had higher concentrations than air from the continent.[79] It is also in line with an earlier study[80] reporting GEM concentrations at two sites in New Hampshire during a powerful nor'easter (*i.e.*, wintertime mid-latitude cyclonic storm) and identifying a clear marine source of GEM. Additionally, Song *et al.*[19] suggested that the Northwest Atlantic Ocean may be a net source of Hg due to peaks in anthropogenic emissions on the east coast of North America and Europe in the 1960–70 s (ref. 81) while Bieser and Schrum[82] showed that coastal GEM concentrations in the Baltic Sea region are increased by up to 10% on annual average due to oceanic evasion. Another hypothesis is that the main source of emissions leading to elevated GEM concentrations during easterly winds is land emissions building up as air recirculates due to sea breezes. Sea breeze is driven by diurnally uneven heating in coastal regions, with warmer (cooler) temperatures over land than over water during the day (at night).[83] As a result, air flows from the sea to the land at low altitude (<500 m), rotating clockwise under the influence of the Coriolis force. The sea breeze, most common in summer, can thus bring back ashore land-originating polluted air.[84,85] This effect is commonly observed at the BU site, where ambient concentrations of local air pollutants tend to increase under sea breeze conditions.[86]

We investigated these hypotheses with the HYSPLIT analysis. The HYSPLIT footprints showed that 34% of the footprint was over the ocean during the growing season (May to September), compared to 11% during the dormant season (November to March). However, because our prior estimate had emissions of ~3–20 ng m^{-2} h^{-1} over land compared to 0.6 ng m^{-2} h^{-1} over the ocean, the contribution to GEM concentrations from ocean emissions was much less than the fractional contribution from the ocean footprint. To assess the impact of land *vs.* ocean emissions on measured GEM, we first optimized land emissions in the Greater Boston area separately for days with average particle exit angle of 200–350° as well as less than 10% of the total footprint over ocean grid cells. We calculated a scaling factor which could be multiplied by land emissions only to best match observed GEM concentrations in Boston during times of only land influence. Model ΔGEM based on optimized land emissions (zero ocean emission) is shown in Fig. 9 (green). The plot shown is based on the ACES prior, but the two priors produced similar results. We then optimized ocean emissions during times with a significant ocean footprint to account for any observed ΔGEM not accounted for by the optimized land emissions. Optimized emissions from land + ocean are shown in blue. Times when the blue and green lines diverge had larger ocean footprints and therefore larger influence of ocean emissions. We find that land-based emissions by themselves can account for nearly all of the GEM observed in Boston. The model is able to reproduce elevated GEM concentrations during oceanic winds with >98% of GEM emissions coming from land grid cells. Although oceanic winds produce a significant footprint over the ocean, there is also a large enough footprint over land, which, combined with low wind speeds and recirculation, accounts for almost all of the GEM observed.

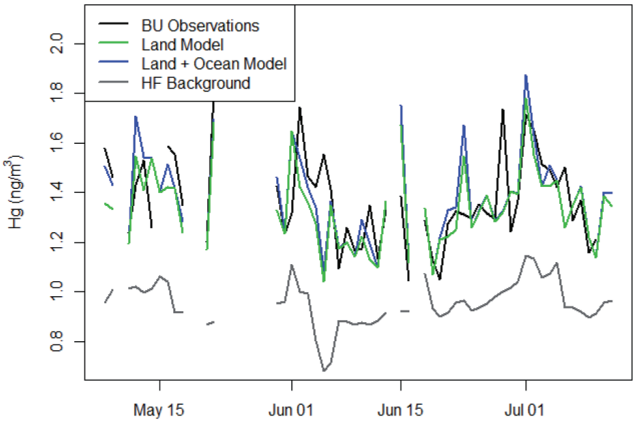

Fig. 9 Daily afternoon average observed GEM at Boston University (BU), GEM at BU modeled using HYSPLIT, and background GEM at Harvard Forest (HF) for May–July 2018. Optimized model GEM based on land emissions only is in green, and based on both land and ocean emissions is in blue.

We therefore find that the elevated GEM concentrations observed during oceanic winds can be fully explained by low wind speeds and at times recirculating air allowing for accumulation of land-based GEM emissions. The significant land influence at the BU site, even during oceanic winds, made it impossible to constrain the scale of ocean emissions. To better investigate the importance of ocean GEM emissions, studies should focus on observations made closer to the ocean, and

more removed from significant sources of land-based emissions.

4. Conclusion

GEM monitoring in the city of Boston from August 2017 to April 2019 shows that ambient air concentrations were within the range of values reported at US rural sites and at the low end of the range reported in the Northern Hemisphere (median of 1.37 ng m^{-3} over the study period). These relatively low concentrations can likely be attributed to aggressive anthropogenic emission reductions under a regional Hg action plan that led to a ~90% reduction in statewide emissions from 1996 to 2008. However, emissions around Boston are still likely higher than currently reported due to uncertainty in the nonpoint category, which accounts for the majority of emissions in Massachusetts. Using three independent and complementary techniques, we show that current inventories underestimate Hg emission rates in the study area by a factor of 3–7. Our analysis suggests that the influence of nonpoint land-based emissions may be comparable in size to point sources in some regions. While Hg emission inventories are thought to be relatively accurate for sources such as energy and industrial sectors,[8] this study adds to the growing body of literature suggesting that fugitive emissions from unknown point and nonpoint sources must be better constrained to improve emission inventories. These emissions are likely to become relatively more important as major point sources are controlled. In parallel, the marked difference in GEM concentration as a function of wind direction prompted us to explore the sources of Hg emissions during oceanic winds. We show that land emissions recirculating due to the sea breeze effect can explain higher concentrations at the monitoring site during oceanic winds. Due to the location of the sampling site, ocean emissions are inextricable from urban emissions. Measurements nearer the ocean and removed from urban influence would be necessary to constrain ocean reemissions accurately.

Conflicts of interest

There are no conflicts to declare.

Acknowledgements

The authors would like to thank Niloptal Ghosh, Ian Smith, Joel Sparks, Pamela Templer, and Cédric Fichot for logistic help at the Boston University site, and Michael Tate and Sarah Janssen for the analysis of the filters at the USGS Mercury Research Laboratory. HA also acknowledges Sae-Yun Kwon for the help installing the Hg instrument and Mark Olson, AMNet site liaison, for troubleshooting assistance. ER's undergraduate research was supported by the EAPS David P. Bacon Fund. HA received financial support from the Swiss National Science Foundation (grant no. 200021_188478) to finalize the manuscript.

References

1 N. E. Selin, Global Biogeochemical Cycling of Mercury: A Review, *Annual Review of Environment and Resources*, 2009, **34**(1), 43–63.
2 D. G. Streets, H. M. Horowitz, Z. Lu, L. Levin, C. P. Thackray and E. M. Sunderland, Five hundred years of anthropogenic mercury: spatial and temporal release profiles, *Environ. Res. Lett.*, 2019, **14**(8), 084004.
3 UNEP, Global Mercury Assessment 2018, 2019, cited 2019 Sep 27, available from, https://wedocs.unep.org/handle/20.500.11822/27579.
4 P. M. Outridge, R. P. Mason, F. Wang, S. Guerrero and L. E. Heimbürger-Boavida, Updated Global and Oceanic Mercury Budgets for the United Nations Global Mercury Assessment 2018, *Environ. Sci. Technol.*, 2018, **52**(20), 11466–11477.
5 D. Obrist, J. L. Kirk, L. Zhang, E. M. Sunderland, M. Jiskra and N. E. Selin, A review of global environmental mercury processes in response to human and natural perturbations: Changes of emissions, climate, and land use, *Ambio*, 2018, **47**(2), 116–140.
6 C. H. Lamborg, C. R. Hammerschmidt, K. L. Bowman, G. J. Swarr, K. M. Munson, D. C. Ohnemus, *et al.*, A global ocean inventory of anthropogenic mercury based on water column measurements, *Nature*, 2014, **512**(65), 65–69.
7 UNEP, Text of the Minamata Convention on Mercury, available at, http://mercuryconvention.org/Portals/11/documents/Booklets/COP1%20version/Minamata-Convention-booklet-eng-full.pdf, last access: 18 April 2018. 2017.
8 H. Selin, S. E. Keane, S. Wang, N. E. Selin, K. Davis and D. Bally, Linking science and policy to support the implementation of the Minamata Convention on Mercury, *Ambio*, 2018, **47**(2), 198–215.
9 J. M. Pacyna, O. Travnikov, F. De Simone, I. M. Hedgecock, K. Sundseth, E. G. Pacyna, *et al.*, Current and future levels of mercury atmospheric pollution on a global scale, *Atmos. Chem. Phys.*, 2016, **16**(19), 12495–12511.
10 D. G. Streets, H. M. Horowitz, Z. Lu, L. Levin, C. P. Thackray and E. Sunderland, Five hundred years of anthropogenic mercury: spatial and temporal release profiles, *Environ. Res. Lett.*, 2019, **14**, 084004.
11 US EPA O, *Basic Information about Mercury and Air Toxics Standards*, US EPA, 2015, cited 2019 Sep 26, available from, https://www.epa.gov/mats/basic-information-about-mercury-and-air-toxics-standards.
12 US EPA O, *2017 National Emissions Inventory (NEI) Data*, US EPA, 2017, cited 2021 Feb 7, available from, https://www.epa.gov/air-emissions-inventories/2017-national-emissions-inventory-nei-data.
13 H. Zhou, C. Zhou, M. M. Lynam, J. T. Dvonch, J. A. Barres, P. K. Hopke, *et al.*, Atmospheric Mercury Temporal Trends in the Northeastern United States from 1992 to 2014: Are Measured Concentrations Responding to Decreasing

Regional Emissions?, *Environ. Sci. Technol. Lett.*, 2017, **4**(3), 91–97.

14 F. Slemr, E.-G. Brunke, R. Ebinghaus and J. Kuss, Worldwide trend of atmospheric mercury since 1995, *Atmos. Chem. Phys.*, 2011, **11**, 4779–4787.

15 A. L. Soerensen, D. J. Jacob, D. G. Streets, M. L. I. Witt, R. Ebinghaus, R. P. Mason, *et al.*, Multi-decadal decline of mercury in the North Atlantic atmosphere explained by changing subsurface seawater concentrations, *Geophys. Res. Lett.*, 2012, **39**, L21810.

16 A. S. Cole, A. Steffen, C. S. Eckley, J. Narayan, M. Pilote, R. Tordon, *et al.*, A survey of mercury in air and precipitation across Canada: patterns and trends, *Atmosphere*, 2014, **5**, 635–668.

17 Y. Zhang, D. J. Jacob, H. M. Horowitz, L. Chen, H. M. Amos, D. P. Krabbenhoft, *et al.*, Observed decrease in atmospheric mercury explained by global decline in anthropogenic emissions, *Proc. Natl. Acad. Sci. U. S. A.*, 2016, **113**(3), 526–531.

18 AMAP/UN Environnement, Technical Background Report for the Global Mercury Assessment 2018, Arctic Monitoring and Assessment Programme, Oslo, Norway/UN Environnement Programme, Chemicals and Health Branch, Geneva, Switzerland; 2019, cited 2019 Sep 27, p. viii + 426 pp including E-Annexes, available from, https://www.amap.no/documents/doc/Technical-Background-Report-for-the-Global-Mercury-Assessment-2018/1815.

19 S. Song, N. E. Selin, L. E. Gratz, J. L. Ambrose, D. A. Jaffe, V. Shah, *et al.*, Constraints from observations and modeling on atmosphere–surface exchange of mercury in eastern North America, *Elementa: Science of the Anthropocene*, 2016, **4**, 000100.

20 D. S. McLagan, B. A. Hussain, H. Huang, Y. D. Lei, F. Wania and C. P. J. Mitchell, Identifying and evaluating urban mercury emission sources through passive sampler-based mapping of atmospheric concentrations, *Environ. Res. Lett.*, 2018, **13**(7), 074008.

21 A. P. Rutter, J. J. Schauer, G. C. Lough, D. C. Snyder, C. J. Kolb, S. V. Klooster, *et al.*, A comparison of speciated atmospheric mercury at an urban center and an upwind rural location, *J. Environ. Monit.*, 2008, **10**(1), 102–108.

22 D. A. Gay, D. Schmeltz, E. Prestbo, M. Olson, T. Sharac and R. Tordon, The Atmospheric Mercury Network: measurement and initial examination of an ongoing atmospheric mercury record across North America, *Atmos. Chem. Phys.*, 2013, **13**(22), 11339–11349.

23 F. Sprovieri, N. Pirrone, M. Bencardino, F. D'Amore, F. Carbone, S. Cinnirella, *et al.*, Atmospheric mercury concentrations observed at ground-based monitoring sites globally distributed in the framework of the GMOS network, *Atmos. Chem. Phys.*, 2016, **16**(18), 11915–11935.

24 P. C. Swartzendruber, D. A. Jaffe and B. Finley, Improved fluorescence peak integration in the Tekran 2537 for applications with sub-optimal sample loadings, *Atmos. Environ.*, 2009, **43**(22), 3648–3651.

25 F. Slemr, A. Weigelt, R. Ebinghaus, H. H. Kock, J. Bödewadt, C. A. M. Brenninkmeijer, *et al.*, Atmospheric mercury measurements onboard the CARIBIC passenger aircraft, *Atmos. Meas. Tech.*, 2016, **9**(5), 2291–2302.

26 J. L. Ambrose, Improved methods for signal processing in measurements of mercury by Tekran® 2537A and 2537B instruments, *Atmos. Meas. Tech.*, 2017, **10**(12), 5063–5073.

27 F. Slemr, A. Weigelt, R. Ebinghaus, J. Bieser, C. A. M. Brenninkmeijer, A. Rauthe-Schöch, *et al.*, Mercury distribution in the upper troposphere and lowermost stratosphere according to measurements by the IAGOS-CARIBIC observatory: 2014–2016, *Atmos. Chem. Phys.*, 2018, **18**(16), 12329–12343.

28 R. Dumarey, E. Temmerman, R. Dams and J. Hoste, The accuracy of the vapour injection calibration method for the determination of mercury by amalgamation/cold vapour atomic spectrometry, *Anal. Chim. Acta*, 1985, **170**, 337–340.

29 J. Huang, M. B. Miller, P. Weiss-Penzias and M. S. Gustin, Comparison of Gaseous Oxidized Hg Measured by KCl-Coated Denuders, and Nylon and Cation Exchange Membranes, *Environ. Sci. Technol.*, 2013, **47**(13), 7307–7316.

30 J. Huang and M. S. Gustin, Uncertainties of Gaseous Oxidized Mercury Measurements Using KCl-Coated Denuders, Cation-Exchange Membranes, and Nylon Membranes: Humidity Influences, *Environ. Sci. Technol.*, 2015, **49**(10), 6102–6108.

31 N. Marusczak, J. E. Sonke, X. Fu and M. Jiskra, Tropospheric GOM at the Pic du Midi Observatory—Correcting Bias in Denuder Based Observations, *Environ. Sci. Technol.*, 2017, **51**(2), 863–869.

32 J. Huang, M. B. Miller, E. Edgerton and M. Sexauer Gustin, Deciphering potential chemical compounds of gaseous oxidized mercury in Florida, USA, *Atmos. Chem. Phys.*, 2017, **17**(3), 1689–1698.

33 M. S. Gustin, J. Huang, M. B. Miller, C. Peterson, D. A. Jaffe, J. Ambrose, *et al.*, Do we understand what the mercury speciation instruments are actually measuring? Results of RAMIX, *Environ. Sci. Technol.*, 2013, **47**, 7295–7306.

34 A. Luippold, M. S. Gustin, S. M. Dunham-Cheatham and L. Zhang, Improvement of quantification and identification of atmospheric reactive mercury, *Atmos. Environ.*, 2020, **224**, 117307.

35 D. Obrist, E. M. Roy, J. L. Harrison, C. F. Kwong, J. W. Munger, H. Moosmüller, *et al.*, Previously unaccounted atmospheric mercury deposition in a midlatitude deciduous forest, *Proc. Natl. Acad. Sci. U. S. A.*, 2021, **118**(29), e2105477118.

36 M. A. Engle, M. T. Tate, D. P. Krabbenhoft, J. J. Schauer, J. B. Kolker, *et al.*, Comparison of atmospheric mercury speciation and deposition at nine sites across central and eastern North America, *J. Geophys. Res.*, 2010, **115**, D18306, DOI: 10.1029/2010JD014064.

37 B. M. Briber, L. R. Hutyra, A. L. Dunn, S. M. Raciti and J. W. Munger, Variations in Atmospheric CO2 Mixing Ratios across a Boston, MA Urban to Rural Gradient, *Land*, 2013, **2**(3), 304–327.

38 M. Sargent, Y. Barrera, T. Nehrkorn, L. R. Hutyra, C. K. Gately, T. Jones, *et al.*, Anthropogenic and biogenic

CO2 fluxes in the Boston urban region, *Proc. Natl. Acad. Sci. U. S. A.*, 2018, 201803715.

39 US EPA, Aqdmrs, 2019, cited 2019 Oct 4, available from, https://aqs.epa.gov/api.

40 S. G. Benjamin, S. S. Weygandt, J. M. Brown, M. Hu, C. R. Alexander, T. G. Smirnova, *et al.*, A North American Hourly Assimilation and Model Forecast Cycle: The Rapid Refresh, *Mon. Weather Rev.*, 2015, **144**(4), 1669–1694.

41 B. Denzler, C. Bogdal, C. Kern, A. Tobler, J. Huo and K. Hungerbühler, Urban source term estimation for mercury using a boundary-layer budget method, *Atmos. Chem. Phys.*, 2019, **19**, 3821–3831.

42 GEOS-Chem horizontal grids – Geos-chem, cited 2019 Aug 9, available from, http://wiki.seas.harvard.edu/geos-chem/index.php/GEOS-Chem_horizontal_grids#0.5_x_0.625_NA_nested_grid.

43 US EPA, *2014 National Emissions Inventory (NEI) Data*, US EPA, 2016, cited 2019 Aug 9, available from, https://www.epa.gov/air-emissions-inventories/2014-national-emissions-inventory-nei-data.

44 W. H. Schroeder, G. Yarwood and H. Niki, Transformation processes involving mercury species in the atmosphere - results from a literature survey, *Water, Air, Soil Pollut.*, 1991, **56**(1), 653–666.

45 Y. Zhang, D. J. Jacob, S. Dutkiewicz, H. M. Amos, M. S. Long and E. M. Sunderland, Biogeochemical drivers of the fate of riverine mercury discharged to the global and Arctic oceans, *Global Biogeochem. Cycles*, 2015, **29**, 854–864.

46 H. M. Horowitz, D. J. Jacob, Y. Zhang, T. S. Dibble, F. Slemr, H. M. Amos, *et al.*, A new mechanism for atmospheric mercury redox chemistry: implications for the global mercury budget, *Atmos. Chem. Phys.*, 2017, **17**(10), 6353–6371.

47 A. F. Stein, R. R. Draxler, G. D. Rolph, B. J. B. Stunder, M. D. Cohen and F. Ngan, NOAA's HYSPLIT Atmospheric Transport and Dispersion Modeling System, *Bull. Am. Meteorol. Soc.*, 2015, **96**(12), 2059–2077.

48 K. McKain, S. C. Wofsy, T. Nehrkorn, J. Eluszkiewicz, J. R. Ehleringer and B. B. Stephens, Assessment of ground-based atmospheric observations for verification of greenhouse gas emissions from an urban region, *Proc. Natl. Acad. Sci. U. S. A.*, 2012, **109**(22), 8423–8428.

49 C. K. Gately and L. R. Hutyra, Large Uncertainties in Urban-Scale Carbon Emissions, *J. Geophys. Res.: Atmos.*, 2017, **122**(20), 11242–11260.

50 Smoke From Siberian Wildfires Invades Northeastern U.S., The Weather Channel – Articles from The Weather Channel, The Weather Channel. cited 2021 Feb 10, available from, https://weather.com/news/news/2018-07-11-smoke-siberian-wildfires-invades-northeast-united-states.

51 A. Gettelman, M. J. Mills, D. E. Kinnison, R. R. Garcia, A. K. Smith, D. R. Marsh, *et al.*, The Whole Atmosphere Community Climate Model Version 6 (WACCM6), *J. Geophys. Res.: Atmos.*, 2019, **124**(23), 12380–12403.

52 M. Jiskra, J. E. Sonke, D. Obrist, J. Bieser, R. Ebinghaus, C. L. Myhre, *et al.*, A vegetation control on seasonal variations in global atmospheric mercury concentrations, *Nat. Geosci.*, 2018, **11**(4), 244–250.

53 L. Xu, J. Chen, L. Yang, Z. Niu, L. Tong, L. Yin, *et al.*, Characteristics and sources of atmospheric mercury speciation in a coastal city, Xiamen, China, *Chemosphere*, 2015, **119**, 530–539.

54 X. Fu, X. Feng, G. Qiu, L. Shang and H. Zhang, Speciated atmospheric mercury and its potential source in Guiyang, China, *Atmos. Environ.*, 2011, **45**(25), 4205–4212.

55 A. Luippold, M. S. Gustin, S. M. Dunham-Cheatham, M. Castro, W. Luke, S. Lyman, *et al.*, Use of Multiple Lines of Evidence to Understand Reactive Mercury Concentrations and Chemistry in Hawai'i, Nevada, Maryland, and Utah, USA, *Environ. Sci. Technol.*, 2020, **54**(13), 7922–7931.

56 X. W. Fu, X. Feng, P. Liang, Deliger, H. Zhang, J. Ji, *et al.*, Temporal trend and sources of speciated atmospheric mercury at Waliguan GAW station, Northwestern China, *Atmos. Chem. Phys.*, 2012, **12**(4), 1951–1964.

57 L. Poissant, M. Pilote, C. Beauvais, P. Constant and H. H. Zhang, A year of continuous measurements of three atmospheric mercury species (GEM, RGM and Hgp) in southern Québec, Canada, *Atmos. Environ.*, 2005, **39**(7), 1275–1287.

58 L. Zhang, L. Wang, S. Wang, H. Dou, J. Li, S. Li, *et al.*, Characteristics and Sources of Speciated Atmospheric Mercury at a Coastal Site in the East China Sea Region, *Aerosol Air Qual. Res.*, 2017, **17**(12), 2913–2923.

59 US EPA, *2011 National Emissions Inventory (NEI) Data*, US EPA, 2015, cited 2018 May 8, available from, https://www.epa.gov/air-emissions-inventories/2011-national-emissions-inventory-nei-data.

60 C. M. Smith and L. J. Trip, Mercury Policy and Science in Northeastern North America: The Mercury Action Plan of the New England Governors and Eastern Canadian Premiers, *Ecotoxicology*, 2005, **14**(1–2), 19–35.

61 NESCAUM. *Massachusetts State Anthropogenic Mercury Emissions Inventory Update — NESCAUM*, 2011, cited 2019 Aug 13, available from, http://www.nescaum.org/documents/ma-hg-inventory-update-201112-final.pdf/view.

62 *In Somerset, Last Coal-Burning Power Plant In Mass. Shuts Down*, cited 2020 Jan 12, available from, https://www.wbur.org/bostonomix/2017/05/31/brayton-power-plant-somerset.

63 X. Lan, R. Talbot, M. Castro, K. Perry and W. Luke, Seasonal and diurnal variations of atmospheric mercury across the US determined from AMNet monitoring data, *Atmos. Chem. Phys.*, 2012, **12**(21), 10569–10582.

64 U. S. Nair, Y. Wu, J. Walters, J. Jansen and E. S. Edgerton, Diurnal and seasonal variation of mercury species at coastal-suburban, urban, and rural sites in the southeastern United States, *Atmos. Environ.*, 2012, **47**, 499–508.

65 M. L. Aucott, A. D. Caldarelli, R. R. Zsolway, C. B. Pietarinen and R. England, Ambient elemental, reactive gaseous, and particle-bound mercury concentrations in New Jersey, U.S.:

measurements and associations with wind direction, *Environ. Monit. Assess.*, 2009, **158**(1–4), 295–306.

66 K. McKain, A. Down, S. M. Raciti, J. Budney, L. R. Hutyra, C. Floerchinger, *et al.*, Methane emissions from natural gas infrastructure and use in the urban region of Boston, Massachusetts, *Proc. Natl. Acad. Sci. U. S. A.*, 2015, **112**(7), 1941–1946.

67 X. Lee, B. O. Russell and J. Andres Robert, Anthropogenic emission of mercury to the atmosphere in the northeast United States, *Geophys. Res. Lett.*, 2001, **28**(7), 1231–1234.

68 C. H. Conaway, R. P. Mason, D. J. Steding and A. R. Flegal, Estimate of mercury emission from gasoline and diesel fuel consumption, San Francisco Bay area, California, *Atmos. Environ.*, 2005, **39**, 101–105.

69 Y. Zhang, H. Horowitz, J. Wang, Z. Xie, J. Kuss and A. L. Soerensen, A Coupled Global Atmosphere-Ocean Model for Air-Sea Exchange of Mercury: Insights into Wet Deposition and Atmospheric Redox Chemistry, *Environ. Sci. Technol.*, 2019, **53**(9), 5052–5061.

70 H. M. Horowitz, D. J. Jacob, H. M. Amos, D. G. Streets and E. M. Sunderland, Historical Mercury Releases from Commercial Products: Global Environmental Implications, *Environ. Sci. Technol.*, 2014, **48**(17), 10242–10250.

71 J. L. Ambrose, L. E. Gratz, D. A. Jaffe, T. Campos, F. M. Flocke, D. J. Knapp, *et al.*, Mercury Emission Ratios from Coal-Fired Power Plants in the Southeastern United States during NOMADSS, *Environ. Sci. Technol.*, 2015, **49**(17), 10389–10397.

72 L. E. Gratz, J. L. Ambrose, D. A. Jaffe, C. Knote, L. Jaeglé, N. E. Selin, *et al.*, Airborne observations of mercury emissions from the Chicago/Gary urban/industrial area during the 2013 NOMADSS campaign, *Atmos. Environ.*, 2016, **145**, 415–423.

73 P. S. Weiss-Penzias, E. J. Williams, B. M. Lerner, T. S. Bates, C. Gaston, K. Prather, *et al.*, Shipboard measurements of gaseous elemental mercury along the coast of Central and Southern California, *J. Geophys. Res.: Atmos.*, 2013, **118**(1), 208–219.

74 G. E. Millward and J. H. Griffin, Concentrations of particulate mercury in the Atlantic marine atmosphere, *Sci. Total Environ.*, 1980, **16**(3), 239–248.

75 A. D. Venter, J. P. Beukes, P. G. van Zyl, E.-G. Brunke, C. Labuschagne, F. Slemr, *et al.*, Statistical exploration of gaseous elemental mercury (GEM) measured at Cape Point from 2007 to 2011, *Atmos. Chem. Phys.*, 2015, **15**(18), 10271–10280.

76 H. Hoglind, S. Eriksson and K. Gardfeldt, Ship-Based Measurements of Atmospheric Mercury Concentrations over the Baltic Sea, *Atmosphere*, 2018, **9**(2), 56.

77 S. J. Smith, H. Pitcher and T. M. L. Wigley, Global and regional anthropogenic sulfur dioxide emissions, *Global and Planetary Change*, 2001, **29**(1), 99–119.

78 D. I. Stern, Global sulfur emissions from 1850 to 2000, *Chemosphere*, 2005, **58**(2), 163–175.

79 I. Cheng, L. Zhang, H. Mao, P. Blanchard, R. Tordon and J. Dalziel, Seasonal and diurnal patterns of speciated atmospheric mercury at a coastal-rural and a coastal-urban site, *Atmos. Environ.*, 2014, **82**, 193–205.

80 J. M. Sigler, H. Mao, B. C. Sive and R. Talbot, Oceanic influence on atmospheric mercury at coastal and inland sites: a springtime noreaster in New England, *Atmos. Chem. Phys.*, 2009, **9**(12), 4023–4030.

81 E. M. Sunderland and R. P. Mason, Human impacts on open ocean mercury concentrations, *Global Biogeochem. Cycles*, 2007, **21**(4), GB4022.

82 J. Bieser and C. Schrum, Impact of marine mercury cycling on coastal atmospheric mercury concentrations in the North- and Baltic Sea region, *Elementa: Science of the Anthropocene*, 2016, **4**, 000111.

83 J. E. Simpson, *Sea Breeze and Local Winds*, Cambridge University Press, 1994, p. 260.

84 D. Baumgardner, G. B. Raga, M. Grutter, G. Lammel and M. Moya, Evolution of anthropogenic aerosols in the coastal town of Salina Cruz, Mexico: Part II particulate phase chemistry, *Sci. Total Environ.*, 2006, **372**(1), 287–298.

85 H. Flocas, A. Kelessis, C. Helmis, M. Petrakakis, M. Zoumakis and K. Pappas, Synoptic and local scale atmospheric circulation associated with air pollution episodes in an urban Mediterranean area, *Theoretical and Applied Climatology*, 2009, **95**(3), 265–277.

86 J. A. Geddes, *Air quality in a coastal urban area*, Geddes *et al.*, Submitted, 2021, 2021, cited 2021 Aug 23, available from, https://open.bu.edu/handle/2144/42891.

87 D. Carslaw and K. Ropkins, openair - An R package for air quality data analysis, *Environmental Modelling & Software*, 2012, **27–28**, 52–61.